Coplanar Waveguide Resonators for Circuit Quantum Electrodynamics

M. Göppl, A. Fragner, M. Baur, R. Bianchetti, S. Filipp, J. M. Fink, P. J. Leek, G. Puebla, L. Steffen, and A. Wallraff
Department of Physics, ETH Zürich, CH-8093, Zürich, Switzerland.
(Dated: July 29, 2008)

We have designed and fabricated superconducting coplanar waveguide resonators with fundamental frequencies from 2 to 9 GHz and loaded quality factors ranging from a few hundreds to a several hundred thousands reached at temperatures of 20 mK. The loaded quality factors are controlled by appropriately designed input and output coupling capacitors. The measured transmission spectra are analyzed using both a lumped element model and a distributed element transmission matrix method. The experimentally determined resonance frequencies, quality factors and insertion losses are fully and consistently characterized by the two models for all measured devices. Such resonators find prominent applications in quantum optics and quantum information processing with superconducting electronic circuits and in single photon detectors and parametric amplifiers.

I. INTRODUCTION

Superconducting coplanar waveguide (CPW) resonators find a wide range of applications as radiation detectors in the optical, UV and X-ray frequency range[1–5], in parametric amplifiers[6–8], for magnetic field tunable resonators[7,9,10] and in quantum information and quantum optics experiments[11–22].

In this paper we discuss the use of CPWs in the context of quantum optics and quantum information processing. In the recent past it has been experimentally demonstrated that a single microwave photon stored in a high quality CPW resonator can be coherently coupled to a superconducting quantum two-level system[11]. This possibility has lead to a wide range of novel quantum optics experiments realized in an architecture now known as circuit quantum electrodynamics (QED)[11]. The circuit QED architecture is also successfully employed in quantum information processing[23] for coherent single qubit control[11], for dispersive qubit read-out[12] and for coupling individual qubits to each other using the resonator as a quantum bus[17,20].

Coplanar waveguide resonators have a number of advantageous properties with respect to applications in circuit QED. CPWs can easily be designed to operate at frequencies up to 10 GHz or higher. Their distributed element construction avoids uncontrolled stray inductances and capacitances allowing for better microwave properties than lumped element resonators. In comparison to other distributed element resonators, such as those based on microstrip lines, the impedance of CPWs can be controlled at different lateral size scales from millimeters down to micrometers not significantly constrained by substrate properties. Their potentially small lateral dimensions allow to realize resonators with extremely large vacuum fields due to electromagnetic zero-point fluctuations[24], a key ingredient for realizing strong coupling between photons and qubits in the circuit QED architecture. Moreover, CPW resonators with large internal quality factors of typically several hundred thousands can now be routinely realized[25–28].

In this paper we demonstrate that we are able to design, fabricate and characterize CPW resonators with well defined resonance frequency and coupled quality factors. The resonance frequency is controlled by the resonator length and its loaded quality factor is controlled by its capacitive coupling to input and output transmission lines. Strongly coupled (overcoupled) resonators with accordingly low quality factors are ideal for performing fast measurements of the state of a qubit integrated into the resonator[12,29]. On the other hand, undercoupled resonators with large quality factors can be used to store photons in the cavity on a long time scale, with potential use as a quantum memory[30].

The paper is structured as follows. In Sec. II we discuss the chosen CPW device geometry, its fabrication and the measurement techniques used for characterization at microwave frequencies. The dependence of the CPW resonator frequency on the device geometry and its electrical parameters is analyzed in Sec. III. In Sec. IV the effect of the resonator coupling to an input/output line on its quality factor, insertion loss and resonance frequency is analyzed using a parallel LCR circuit model. This lumped element model provides simple approximations of the resonator properties around resonance and allows to develop an intuitive understanding of the device. We also make use of the transmission (or ABCD) matrix method to describe the full transmission spectrum of the resonators and compare its predictions to our experimental data. The characteristic properties of the higher harmonic modes of the CPW resonators are discussed in Sec. V.

II. DEVICE GEOMETRY, FABRICATION AND MEASUREMENT TECHNIQUE

The planar geometry of a capacitively coupled CPW resonator is sketched in Figure 1a. The resonator is formed of a center conductor of width $w = 10\,\mu$m separated from the lateral ground planes by a gap of width $s = 6.6\,\mu$m. Resonators with various center conductor lengths l between 8 and 29 mm aiming at fundamental frequencies f_0 between 2 and 9 GHz were designed. These structures are easily fabricated in optical lithography while providing sufficiently large vacuum

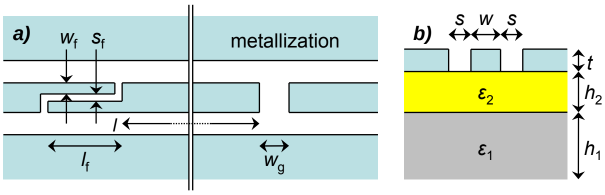

FIG. 1: (Color online) (a) Top view of a CPW resonator with finger capacitors (l.h.s.) and gap capacitors (r.h.s.). (b) Cross section of a CPW resonator design. Center conductor and lateral ground metallization (blue) on top of a double layer substrate (grey/yellow). Parameters are discussed in the main text.

field strengths[24]. The center conductor is coupled via gap- or finger capacitors to the input and output transmission lines. For small coupling capacitances gap capacitors of widths $w_{\mathrm{g}} = 10$ to $50\,\mu$m have been realized. To achieve larger coupling, finger capacitors formed by from one up to eight pairs of fingers of length $l_{\mathrm{f}} = 100\,\mu$m, width $w_{\mathrm{f}} = 3.3\,\mu$m and separation $s_{\mathrm{f}} = 3.3\,\mu$m have been designed and fabricated, see Fig. 1.

The resonators are fabricated on high resistivity, undoped, (100)-oriented, thermally oxidized two inch silicon wafers. The oxide thickness is $h_2 = 550\,\mathrm{nm} \pm 50\,\mathrm{nm}$ determined by SEM inspection. The bulk resistivity of the Si wafer is $\rho > 3000\,\Omega\,\mathrm{cm}$ determined at room temperature in a van-der-Pauw measurement. The total thickness of the substrate is $h_1 = 500\,\mu\mathrm{m} \pm 25\,\mu\mathrm{m}$. A cross-sectional sketch of the CPW resonator is shown in Fig. 1b.

The resonators were patterned in optical lithography using a one micron thick layer of the negative tone resist ma-N 1410. The substrate was subsequently metallized with a $t = 200\,\mathrm{nm} \pm 5\,\mathrm{nm}$ thick layer of Al, electron beam evaporated at a rate of 5 Å/sec and lifted-off in 50° C hot acetone. Finally, all structures were diced into $2\,\mathrm{mm} \times 7\,\mathrm{mm}$ chips, each containing an individual resonator. The feature sizes of the fabricated devices deviate less than 100 nm from the designed dimensions as determined by SEM inspection indicating a good control over the fabrication process.

Altogether, more than 80 Al CPW resonators covering a wide range of different coupling strengths were designed and fabricated. More than 30 of these devices were carefully characterized at microwave frequencies. Figure 2 shows optical microscope images of the final Al resonators with different finger and gap capacitors.

Using a 40 GHz vector network analyzer, S_{21} transmission measurements of all resonators were performed in a pulse-tube based dilution refrigerator system[31] at temperatures of 20 mK. The measured transmission spectra are plotted in logarithmic units (dB) as $20\log_{10}|S_{21}|$. High Q resonators were measured using a 32 dB gain high electron mobility transistor (HEMT) amplifier with noise temperature of $\sim$5 K installed at the 4 K stage of the refrigerator as well as one or two room temperature

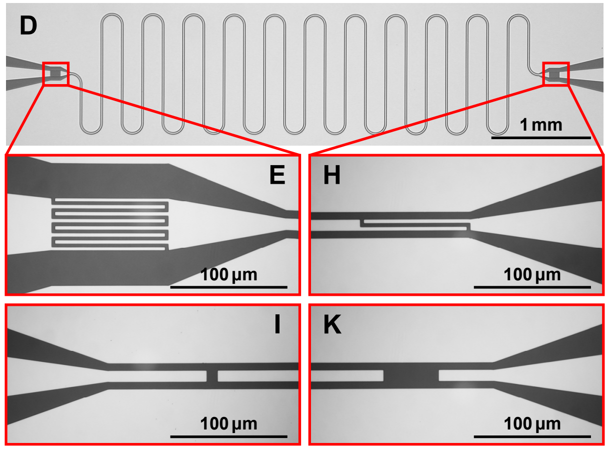

FIG. 2: (Color online) Optical microscope images of an Al coplanar waveguide resonator (white is metallization, grey is substrate). The red squares in the upper image indicate the positions of the input/output capacitors. Also shown are microscope images of finger- and gap capacitor structures. The labels D, E, H, I, K refer to the device ID listed in Tab. II.

amplifiers with 35 dB gain each. Low Q resonators were characterized without additional amplifiers.

The measured Q of undercoupled devices can vary strongly with the power applied to the resonator. In our measurements of high Q devices the resonator transmission spectrum looses its Lorentzian shape at drive powers above approximately -70 dBm at the input port of the resonator due to non-linear effects[32]. At low drive powers, when dielectric resonator losses significantly depend on the photon number inside the cavity[28,33], measured quality factors may be substantially reduced. We acquired S_{21} transmission spectra at power levels chosen to result in the highest measurable quality factors, i.e. at high enough powers to minimize dielectric loss but low enough to avoid non-linearities. This approach has been chosen to be able to focus on geometric properties of the resonators.

III. BASIC RESONATOR PROPERTIES

A typical transmission spectrum of a weakly gap capacitor coupled ($w_g = 10\,\mu$m) CPW resonator of length $l = 14.22$ mm is shown in Figure 3a. The spectrum clearly displays a Lorentzian lineshape of width δf centered at the resonance frequency f_0. Figure 3b shows measured resonance frequencies f_0 for resonators of different length l, all coupled via gap capacitors of widths $w_g = 10\,\mu$m. Table I lists the respective values for l and f_0. For these small capacitors the frequency shift induced by coupling can be neglected, as discussed in a later section. In this case the resonator‘s fundamental frequency f_0 is given by

$$f_0 = \frac{c}{\sqrt{\epsilon_{\mathrm{eff}}}}\frac{1}{2l}. \tag{1}$$

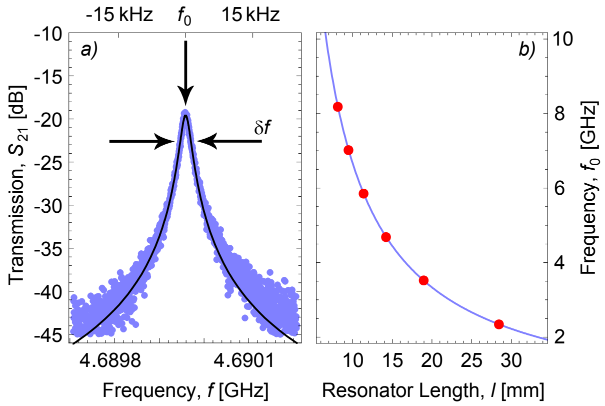

FIG. 3: (Color online) (a) Transmission spectrum of a 4.7 GHz resonator. Data points (blue) were fitted (black) with a Lorentzian line. (b) Measured f_0 (red points) of several resonators coupled via $w_g = 10\,\mu$m gap capacitors with different l together with a fit (blue line) to the data using Eq. (1) as fit function and $\epsilon_{\rm eff}$ as fit parameter.

f_0 (GHz)	l (mm)
2.3430	28.449
3.5199	18.970
4.6846	14.220
5.8491	11.380
7.0162	9.4800
8.1778	8.1300

TABLE I: Designed values for resonator lengths l and measured resonance frequencies f_0, corresponding to the data shown in Fig. 3.

Here, $c/\sqrt{\epsilon_{\rm eff}} = v_{\rm ph}$ is the phase velocity depending on the velocity of light in vacuum c and the effective permittivity $\epsilon_{\rm eff}$ of the CPW line. $\epsilon_{\rm eff}$ is a function of the waveguide geometry and the relative permittivities ϵ_1 and ϵ_2 of substrate and the oxide layer, see Fig. 1b. Furthermore, $2l = \lambda_0$ is the wavelength of the fundamental resonator mode. The length dependence of the measured resonance frequencies f_0 of our samples is well described by Eq. (1) with the effective dielectric constant $\epsilon_{\rm eff} = 5.05$, see Fig. 3b.

The phase velocity $v_{\rm ph} = 1/\sqrt{L_\ell C_\ell}$ of electromagnetic waves propagating along a transmission line depends on the capacitance C_ℓ and inductance L_ℓ per unit length of the line. Using conformal mapping techniques the geometric contribution to L_ℓ and C_ℓ of a CPW line is found to be[34,35]

$$L_\ell = \frac{\mu_0}{4}\frac{K(k_0')}{K(k_0)}, \tag{2}$$

$$C_\ell = 4\epsilon_0\epsilon_{\rm eff}\frac{K(k_0)}{K(k_0')}. \tag{3}$$

Here, K denotes the complete elliptic integral of the first kind with the arguments

$$k_0 = \frac{w}{w+2s}, \tag{4}$$

$$k_0' = \sqrt{1-k_0^2}. \tag{5}$$

ID	Coupling	C_κ (fF)	f_0 (GHz)	$Q_{\rm L}$
A	8 + 8 finger	56.4	2.2678	$3.7 \cdot 10^2$
B	7 + 7 finger	48.6	2.2763	$4.9 \cdot 10^2$
C	6 + 6 finger	42.9	2.2848	$7.5 \cdot 10^2$
D	5 + 5 finger	35.4	2.2943	$1.1 \cdot 10^3$
E	4 + 4 finger	26.4	2.3086	$1.7 \cdot 10^3$
F	3 + 3 finger	18.0	2.3164	$3.9 \cdot 10^3$
G	2 + 2 finger	11.3	2.3259	$9.8 \cdot 10^3$
H	1 + 1 finger	3.98	2.3343	$7.5 \cdot 10^4$
I	10 μm gap	0.44	2.3430	$2.0 \cdot 10^5$
J	20 μm gap	0.38	2.3448	$2.0 \cdot 10^5$
K	30 μm gap	0.32	2.3459	$2.3 \cdot 10^5$
L	50 μm gap	0.24	2.3464	$2.3 \cdot 10^5$

TABLE II: Properties of the different CPW resonators whose transmission spectra are shown in Fig. 4. C_κ denotes the simulated coupling capacitances, f_0 is the measured resonance frequency and $Q_{\rm L}$ is the measured quality factor.

For non magnetic substrates ($\mu_{\rm eff} = 1$) and neglecting kinetic inductance for the moment L_ℓ is determined by the CPW geometry only. C_ℓ depends on the geometry and $\epsilon_{\rm eff}$. Although analytical expressions for $\epsilon_{\rm eff}$ exist for double layer substrates deduced from conformal mapping[34], the accuracy of these calculations depends sensitively on the ratio between substrate layer thicknesses and the dimensions of the CPW cross-section[36] and does not lead to accurate predictions for our parameters. Therefore, we have calculated $C_\ell \approx 1.27 \cdot 10^{-10}\,{\rm Fm}^{-1}$ using a finite element electromagnetic simulation and values $\epsilon_1 = 11.6$ (see Ref. 37) for silicon and $\epsilon_2 = 3.78$ (see Ref. 37) for silicon oxide for our CPW geometry and substrate. From this calculation we find $\epsilon_{\rm eff} \approx 5.22$ which deviates only by about 3% from the value extracted from our measurements. The characteristic impedance of a CPW is then given by $Z_0 = \sqrt{L_\ell/C_\ell}$ which results in a value of 59.7 Ω for our geometry. This value deviates from the usually chosen value of 50 Ω as the original design was optimized for a different substrate material.

In general, for superconductors the inductance L_ℓ is the sum of the temperature independent geometric (magnetic) inductance $L_\ell^{\rm m}$ and the temperature dependent kinetic inductance $L_\ell^{\rm k}$ (see Ref. 38). For superconductors, $L_\ell^{\rm k}$ refers to the inertia of moving Cooper pairs and can contribute significantly to L_ℓ since resistivity is suppressed and thus charge carrier relaxation times are large. According to Ref. 35, $L_\ell^{\rm k}$ scales with $\lambda^2(T)$, where $\lambda(T)$ is the temperature dependent London penetration depth which can be approximated as[35] $\lambda(0) = 1.05 \cdot 10^{-3}\sqrt{\rho(T_{\rm c})/T_{\rm c}}\,\sqrt{{\rm K\,m}/\Omega}$ at zero temperature in the

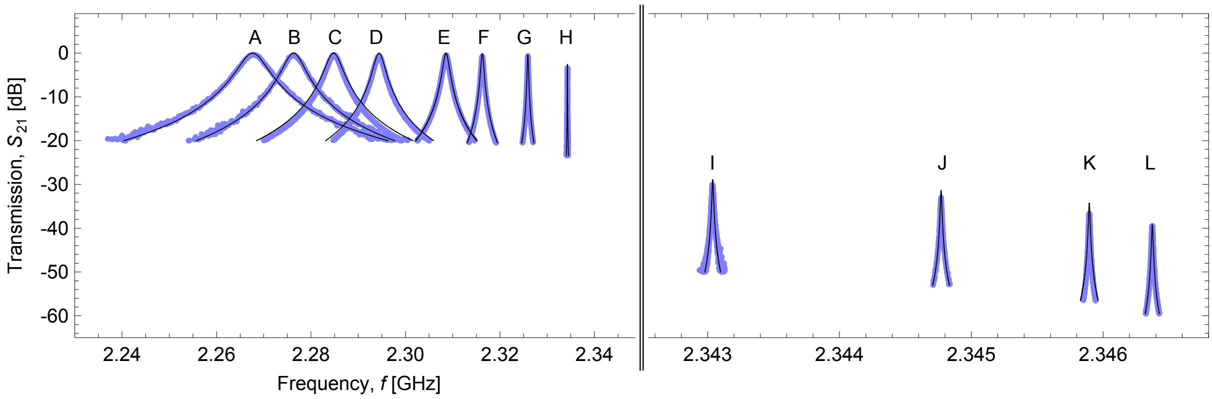

FIG. 4: (Color online) S_{21} transmission spectra of 2.3 GHz resonators, symmetrically coupled to input/output lines. The left part of the split plot shows spectra of finger capacitor coupled resonators whereas on the right hand side one can see spectra of gap capacitor coupled resonators. The data points (blue) were fitted (black) with the transmission matrix method, see text.

local and dirty limits. In the dirty (local) limit the mean free path of electrons l_{mf} is much less than the coherence length $\xi_0 = \hbar v_{\mathrm{f}}/\pi\Delta(0)$, where v_{f} is the Fermi velocity of the electrons and $\Delta(0)$ is the superconducting gap energy at zero temperature[39]. The clean (nonlocal) limit occurs when l_{mf} is much larger than ξ_0 (see Ref. 39). $T_{\mathrm{c}} = 1.23\,\mathrm{K}$ is the critical temperature of our thin film aluminum and $\rho(T_{\mathrm{c}}) = 2.06\cdot 10^{-9}\,\Omega\,\mathrm{m}$ is the normal state resistivity at $T = T_{\mathrm{c}}$. T_{c} and $\rho(T)$ were determined in a four-point measurement of the resistance of a lithographically patterned Al thin film meander structure from the same substrate in dependence on temperature. The resulting residual resistance ratio ($RRR_{300\,\mathrm{K}/1.3\,\mathrm{K}}$) is 8.6. Since our measurements were performed at temperatures well below T_{c}, $\lambda = \lambda(0)$ approximately holds and we find $\lambda(0) \approx 43\,\mathrm{nm}$ for our Al thin films (compared to a value of 40 nm, given in Ref. 40). Using the above approximation shows that L_ℓ^{k} is about two orders of magnitude smaller than $L_\ell^{\mathrm{m}} = 4.53\cdot 10^{-7}\,\mathrm{Hm}^{-1}$ legitimating the assumption $L_\ell \approx L_\ell^{\mathrm{m}}$ made in Eq. (2). Kinetic inductance effects in Niobium resonators are also analyzed in Ref. 25.

IV. INPUT/OUTPUT COUPLING

To study the effect of the capacitive coupling strength on the microwave properties of CPW resonators, twelve 2.3 GHz devices, symmetrically coupled to input/output lines with different gap and finger capacitors have been characterized, see Table II for a list of devices. The measured transmission spectra are shown in Fig. 4. The left hand part of Fig. 4 depicts spectra of resonators coupled via finger capacitors having 8 down to one pairs of fingers (devices A to H). The right hand part of Fig. 4 shows those resonators coupled via gap capacitors with gap widths of $w_g = 10$, 20, 30 and 50 μm (devices I to L) respectively. The coupling capacitance continuously decreases from device A to device L. The nominal values for the coupling capacitance C_κ obtained from EM-simulations for the investigated substrate properties and geometry are listed in table II. The resonance frequency f_0 and the measured quality factor $Q_{\mathrm{L}} = f_0/\delta f$ of the respective device is obtained by fitting a Lorentzian line shape

$$F_{\mathrm{Lor}}(f) = A_0 \frac{\delta f}{(f - f_0)^2 + \delta f^2/4}, \tag{6}$$

to the data, see Fig. 3a, where δf is the full width half maximum of the resonance. With increasing coupling capacitance C_κ, Fig. 4 shows a decrease in the measured (loaded) quality factor Q_{L} and an increase in the peak transmission, as well as a shift of f_0 to lower frequencies. In the following, we demonstrate how these characteristic resonator properties can be fully understood and modeled consistently for the full set of data.

A transmission line resonator is a distributed device with voltages and currents varying in magnitude and phase over its length. The distributed element representation of a symmetrically coupled resonator is shown in Fig. 5a. R_ℓ, L_ℓ and C_ℓ denote the resistance, inductance and capacitance per unit length, respectively. According to Ref. 41 the impedance of a TL resonator is given by

$$Z_{\mathrm{TL}} = Z_0 \frac{1 + i\tan\beta l \tanh\alpha l}{\tanh\alpha l + i\tan\beta l} \tag{7}$$

$$\approx \frac{Z_0}{\alpha l + i\frac{\pi}{\omega_0}(\omega - \omega_{\mathrm{n}})}. \tag{8}$$

α is the attenuation constant and $\beta = \omega_{\mathrm{n}}/v_{\mathrm{ph}}$ is the phase constant of the TL. The approximation in Eq. (8) holds when assuming small losses ($\alpha l \ll 1$) and for ω close to ω_{n}. Here, $\omega_{\mathrm{n}} = n\omega_0 = 1/\sqrt{L_{\mathrm{n}}C}$ is the angular frequency of the n-th mode, where n denotes the resonance mode number ($n = 1$ for the fundamental mode).

Around resonance, the properties of a TL resonator can be approximated by those of a lumped element, parallel

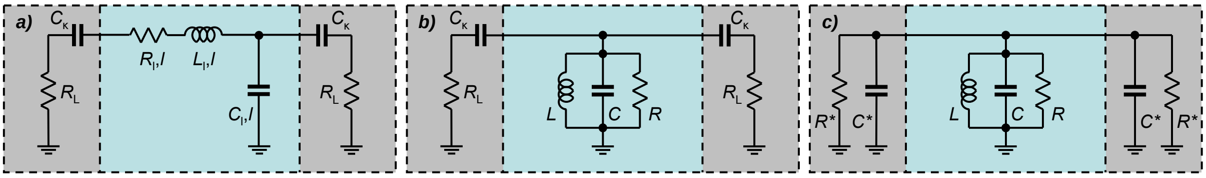

FIG. 5: (Color online) (a) Distributed element representation of symmetrically coupled TL resonator. (b) Parallel LCR oscillator representation of TL resonator. (c) Norton equivalent of symmetrically coupled, parallel LCR oscillator. Symbols are explained in text.

LCR oscillator, as shown in Fig. 5b, with impedance

$$Z_{\mathrm{LCR}} = \left(\frac{1}{i\omega L_{\mathrm{n}}} + i\omega C + \frac{1}{R}\right)^{-1} \quad (9)$$

$$\approx \frac{R}{1 + 2iRC(\omega - \omega_{\mathrm{n}})}, \quad (10)$$

and characteristic parameters

$$L_{\mathrm{n}} = \frac{2L_\ell l}{n^2\pi^2}, \quad (11)$$

$$C = \frac{C_\ell l}{2}, \quad (12)$$

$$R = \frac{Z_0}{\alpha l}. \quad (13)$$

The approximation Eq. (10) is valid for $\omega \approx \omega_{\mathrm{n}}$. The LCR model is useful to get an intuitive understanding of the resonator properties. It simplifies analyzing the effect of coupling the resonator to an input/output line on the quality factor and on the resonance frequency as discussed in the following.

The (internal) quality factor of the parallel LCR oscillator is defined as $Q_{\mathrm{int}} = R\sqrt{C/L_{\mathrm{n}}} = \omega_{\mathrm{n}} RC$. The quality factor Q_L of the resonator coupled with capacitance C_κ to the input and output lines with impedance Z_0 is reduced due to the resistive loading. Additionally, the frequency is shifted because of the capacitive loading of the resonator due to the input/output lines. To understand this effect the series connection of C_κ and R_{L} can be transformed into a Norton equivalent parallel connection of a resistor R^* and a capacitor C^*, see Figs. 5b, c, with

$$R^* = \frac{1 + \omega_{\mathrm{n}}^2 C_\kappa^2 R_{\mathrm{L}}^2}{\omega_{\mathrm{n}}^2 C_\kappa^2 R_{\mathrm{L}}}, \quad (14)$$

$$C^* = \frac{C_\kappa}{1 + \omega_{\mathrm{n}}^2 C_\kappa^2 R_{\mathrm{L}}^2}. \quad (15)$$

The small capacitor C_κ transforms the $R_{\mathrm{L}} = 50\,\Omega$ load into the large impedance $R^* = R_{\mathrm{L}}/k^2$ with $k = \omega_{\mathrm{n}} C_\kappa R_{\mathrm{L}} \ll 1$. For symmetric input/output coupling the loaded quality factor for the parallel combination of R and $R^*/2$ is

$$Q_{\mathrm{L}} = \omega_{\mathrm{n}}^* \frac{C + 2C^*}{1/R + 2/R^*} \quad (16)$$

$$\approx \omega_{\mathrm{n}} \frac{C}{1/R + 2/R^*} \quad (17)$$

with the n-th resonance frequency shifted by the capacitive loading due to the parallel combination of C and $2C^*$

$$\omega_{\mathrm{n}}^* = \frac{1}{\sqrt{L_{\mathrm{n}}(C + 2C^*)}}. \quad (18)$$

For $\omega_{\mathrm{n}}^* \approx \omega_{\mathrm{n}}$ with $C + 2C^* \approx C$, the Norton equivalent expression for the loaded quality factor Q_{L} is a parallel combination of the internal and external quality factors

$$\frac{1}{Q_{\mathrm{L}}} = \frac{1}{Q_{\mathrm{int}}} + \frac{1}{Q_{\mathrm{ext}}}, \quad (19)$$

with

$$Q_{\mathrm{int}} = \omega_{\mathrm{n}} RC = \frac{n\pi}{2\alpha l}, \quad (20)$$

$$Q_{\mathrm{ext}} = \frac{\omega_{\mathrm{n}} R^* C}{2}. \quad (21)$$

The measured loaded quality factor Q_{L} for devices A to L is plotted vs. the coupling capacitance in Fig. 6a. Q_L is observed to be constant for small coupling capacitances and decreases for large ones. In the overcoupled regime ($Q_{\mathrm{ext}} \ll Q_{\mathrm{int}}$), Q_{L} is governed by Q_{ext} which is well approximated by $C/2\omega_{\mathrm{n}} R_{\mathrm{L}} C_\kappa^2$, see dashed line in Fig. 6. Thus, in the overcoupled regime the loaded quality factor $Q_{\mathrm{L}} \propto C_\kappa^{-2}$ can be controlled by the choice of the coupling capacitance. In the undercoupled limit ($Q_{\mathrm{ext}} \gg Q_{\mathrm{int}}$) however, Q_{L} saturates at the internal quality factor $Q_{\mathrm{int}} \approx 2.3 \cdot 10^5$ determined by the intrinsic losses of the resonator, see horizontal dashed line in Fig. 6a.

Radiation losses are expected to be small in CPW resonators[42], resistive losses are negligible well below the critical temperature T_{c} of the superconductor[25] and at frequencies well below the superconducting gap. We believe that dielectric losses limit the internal quality factor of our devices, as discussed in References 33 and 28.

Using Eqs. (14, 19, 21), C_κ has been extracted from the measured value of $Q_{\mathrm{int}} \sim 2.3 \cdot 10^5$ and the measured loaded quality factors Q_{L} of the overcoupled devices A to H, see Fig. 7. The experimental values of C_κ are in good agreement with the ones found from finite element calculations, listed in table II, with a standard deviation of about 4%.

The insertion loss

$$L_0 = -20 \log \left(\frac{g}{g+1}\right) \mathrm{dB} \quad (22)$$

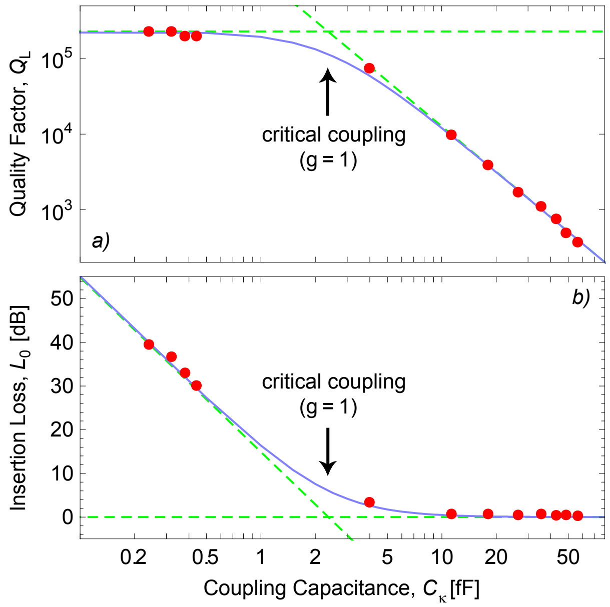

FIG. 6: (Color online) (a) Dependence of Q_{L} on C_κ. Data points (red) are measured quality factors. These values are compared to Q_{L} predictions by the mapped LCR model (solid blue line) given by Eqs. (14, 19, 21). (b) Dependence of L_0 on C_κ. Data points (red) show measured L_0 values. The values are compared to the mapped LCR model (solid blue line) given by Eqs. (14, 21, 22). Dashed lines indicate the limiting cases for small and large coupling capacitances (see text).

of a resonator, i.e. the deviation of peak transmission from unity, is dependent on the ratio of the internal to the external quality factor which is also called the coupling coefficient $g = Q_{\mathrm{int}}/Q_{\mathrm{ext}}$ (see Ref. 41). The measured values of L_0 as extracted from Fig. 4 are shown in Fig. 6b. For $g > 1$ (large C_κ) the resonator is overcoupled and shows near unit transmission ($L_0 = 0$). The resonator is said to be critically coupled for $g = 1$. For $g < 1$ (small C_κ) the resonator is undercoupled and the transmission is significantly reduced. In this case L_0 is well approximated by $-20\log(2\omega_{\mathrm{n}} Q_{\mathrm{int}} R_{\mathrm{L}} C_\kappa^2/C)$, see dashed line in Fig. 6b, as calculated from Eqs. (14, 21, 22). Q_{ext} and Q_{int} can be determined from Q_{L} and L_0 using Eqs. (19, 22), thus allowing to roughly estimate internal losses even of an overcoupled cavity.

For the overcoupled devices A to H the coupling induced resonator frequency shift as extracted from Fig. 4 is in good agreement with calculations based on Eqs. (15, 18), see Fig. 7b. For $C^* \approx C_\kappa$ and $C \gg C_\kappa$ one can Taylor-approximate ω_{n}^* as $\omega_{\mathrm{n}}(1 - C_\kappa/C)$. As a result the relative resonator frequency shift is $(\omega_{\mathrm{n}}^* - \omega_{\mathrm{n}})/\omega_{\mathrm{n}} = -C_\kappa/C$ for symmetric coupling. Figure 7b shows the expected linear dependence with a maximum frequency shift of about 3% over a range of 60 fF in C_κ.

As an alternative method to the LCR model which is only an accurate description near resonance we have analyzed our data using the transmission matrix method[41]. Using this method the full transmission spectrum of the CPW resonator can be calculated. However, because of the mathematical structure of the model it is more involved to gain intuitive understanding of the CPW devices.

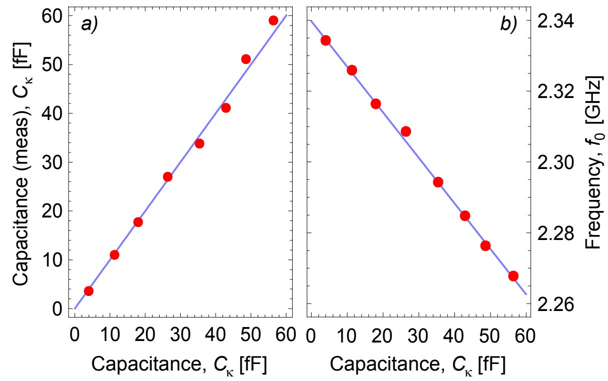

FIG. 7: (Color online) (a) Comparison of C_κ values extracted from the measured quality factors using Eqs. (14, 19, 21) to the EM-simulated values for C_κ (red points) for devices A to H. The blue curve is a line through origin with slope one. (b) Dependence of f_0 on C_κ. The mapped LCR model prediction given by Eqs. (15, 18) is shown (blue line) for resonators coupled via finger capacitors together with the measured values for f_0 (red points).

All measured S_{21} transmission spectra are consistently fit with a single set of parameters, see Fig. 4. The transmission or ABCD matrix of a symmetrically coupled TL is defined by the product of an input-, a transmission-, and an output matrix as

$$\begin{pmatrix} A & B \\ C & D \end{pmatrix} = \begin{pmatrix} 1 & Z_{\mathrm{in}} \\ 0 & 1 \end{pmatrix} \begin{pmatrix} t_{11} & t_{12} \\ t_{21} & t_{22} \end{pmatrix} \begin{pmatrix} 1 & Z_{\mathrm{out}} \\ 0 & 1 \end{pmatrix}, \tag{23}$$

with input/output impedances $Z_{\mathrm{in/out}} = 1/i\omega C_\kappa$ and the transmission matrix parameters

$$\begin{aligned} t_{11} &= \cosh(\gamma l), & (24) \\ t_{12} &= Z_0 \sinh(\gamma l), & (25) \\ t_{21} &= 1/Z_0 \sinh(\gamma l), & (26) \\ t_{22} &= \cosh(\gamma l). & (27) \end{aligned}$$

Here, $\gamma = \alpha + i\beta$ is the TL wave propagation coefficient. The resonator transmission spectrum is then defined by the ABCD matrix components as

$$S_{21} = \frac{2}{A + B/R_{\mathrm{L}} + C R_{\mathrm{L}} + D}. \tag{28}$$

Here, R_{L} is the real part of the load impedance, accounting for outer circuit components. α is determined by Q_{int} and l and β depends on ϵ_{eff} as discussed before. According to Eqs. (2, 3) Z_0 is determined by ϵ_{eff}, w and s. The attenuation constant is $\alpha \sim 2.4 \cdot 10^{-4}\,\mathrm{m}^{-1}$ as determined from $Q_{\mathrm{int}} \sim 2.3 \cdot 10^5$.

For gap capacitor coupled devices, the measured data fits very well, see Fig. 4, to the transmission spectrum calculated using the ABCD matrix method with $\bar{\epsilon}_{\rm eff} = 5.05$, already obtained from the measured dependence of f_0 on the resonator length, see Fig. 3. For finger capacitor coupled structures however, see Fig. 1a, approximately 40% of the length of each 100 μm finger has to be added to the length l of the bare resonators in order to obtain good fits to the resonance frequency f_0. This result is independent of the number of fingers. The ABCD matrix model describes the full transmission spectra of all measured devices very well with a single set of parameters, see Fig. 4.

V. HARMONIC MODES

So far we have only discussed the properties of the fundamental resonance frequency of any of the measured resonators. A full transmission spectrum of the overcoupled resonator D, including 5 harmonic modes, is shown in Fig. 8. The measured spectrum fits well to the ABCD matrix model for the fundamental frequency and also for higher cavity modes, displaying a decrease of the loaded quality factor with harmonic number. The dependence of the measured quality factor $Q_{\rm L}$ on the mode number n is in good agreement with Eqs. (19, 21) and scales approximately as $C/2n\omega_0 R_{\rm L} C_\kappa^2$.

VI. CONCLUSIONS

In summary, we have designed and fabricated symmetrically coupled coplanar waveguide resonators over a wide range of resonance frequencies and coupling strengths. We demonstrate that loaded quality factors and resonance frequencies can be controlled and that the LCR- and ABCD matrix models are in good agreement with measured data for fundamental and harmonic modes. In the case of resonators coupled via finger capacitors simulated values for C_κ deviate by only about 4%. About 40% of the capacitor finger length has to be added to the total resonator length to obtain a good fit to the resonance frequency.

The resonator properties discussed above are consistent with those obtained from measurements of additional devices with fundamental frequencies of 3.5, 4.7, 5.8, 7.0 and 8.2 GHz. The experimental results presented in this paper were obtained for Al based resonators on an oxidized silicon substrate. The methods of analysis should also be applicable to CPW devices fabricated on different substrates and with different superconducting materials. The good understanding of geometric and electrical properties of CPW resonators will certainly foster further research on their use as radiation detectors, in quantum electrodynamics and quantum information processing applications.

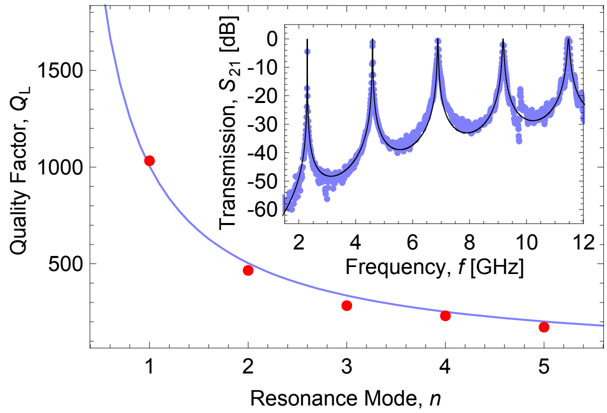

FIG. 8: Measured quality factors for the overcoupled resonator D vs. mode number n (red points) together with the prediction of the mapped LCR model given by Eqs. (18, 21) (solid blue line). The inset shows the S_{21} transmission spectrum of resonator D with fundamental mode and harmonics. The measured data (blue) is compared to the S_{21} spectrum (black) obtained by the ABCD matrix method.

Acknowledgments

We thank P. Fallahi for designing the optical lithography mask used for fabricating the devices and L. Frunzio and R. Schoelkopf at Yale University for their continued collaboration on resonator fabrication and characterization. We also thank the Yale group and the group of M. Siegel at the Institute for Micro- and Nanoelectronic Systems at University of Karlsruhe for exchange of materials and preparation of thin films. Furthermore we acknowledge the ETH Zürich FIRST Center for Micro- and Nanoscience for providing and supporting the device fabrication infrastructure essential for this project. We acknowledge discussions with J. Martinis and K. Lehnert and thank D. Schuster for valuable comments on the manuscript. This work was supported by Swiss National Fund (SNF) and ETH Zürich. P. J. L. was supported by the EC with a MC-EIF.

[1] B. A. Mazin, P. K. Day, H. G. LeDuc, A. Vayonakis, and J. Zmuidzinas, 2002 Proc. SPIE **4849**, 283 (2002).
[2] P. K. Day, H. G. LeDuc, B. A. Mazin, A. Vayonakis, and J. Zmuidzinas, Nature **425**, 817 (2003).
[3] J. Zmuidzinas and P. L. Richards, Proc. IEEE **92(10)**, 1597 (2004).
[4] B. A. Mazin, M. E. Eckart, B. Bumble, S. Golwala, P. Day, J. Gao, and J. Zmuidzinas, J. Low Temp. Phys. **151**, 537

(2008).
[5] G. Vardulakis, S. Withington, D. J. Goldie, and D. M. Glowacka, Meas. Sci. Technol. **19**, 015509 (2008).
[6] E. Tholén, A. Ergül, E. Doherty, F. Weber, F. Grégis, and D. Haviland, Appl. Phys. Lett. **90**, 253509 (2007).
[7] M. Castellanos-Beltran and K. Lehnert, Appl. Phys. Lett. **91**, 083509 (2007).
[8] N. Bergeal, R. Vijay, V. E. Manucharyan, I. Siddiqi, R. J. Schoelkopf, S. M. Girvin, and M. H. Devoret, arXiv.org:0805.3452 (2008).
[9] A. Palacios-Laloy, F. Nguyen, F. Mallet, P. Bertet, D. Vion, and D. Esteve, arXiv:0712.0221v1 (2007).
[10] M. Sandberg, C. Wilson, F. Persson, G. Johansson, V. Shumeiko, T. Duty, and P. Delsing, arXiv:0801.2479v1 (2008).
[11] A. Wallraff, D. I. Schuster, A. Blais, L. Frunzio, R.-S. Huang, J. Majer, S. Kumar, S. M. Girvin, and R. J. Schoelkopf, Nature **431**, 162 (2004).
[12] A. Wallraff, D. I. Schuster, A. Blais, L. Frunzio, J. Majer, S. M. Girvin, and R. J. Schoelkopf, Phys. Rev. Lett. **95**, 060501 (2005).
[13] D. I. Schuster, A. Wallraff, A. Blais, L. Frunzio, R.-S. Huang, J. Majer, S. M. Girvin, and R. J. Schoelkopf, Phys. Rev. Lett. **94**, 123602 (2005).
[14] A. Wallraff, D. I. Schuster, A. Blais, J. M. Gambetta, J. Schreier, L. Frunzio, M. H. Devoret, S. M. Girvin, and R. J. Schoelkopf, Phys. Rev. Lett. **99**, 050501 (2007).
[15] D. I. Schuster, A. A. Houck, J. A. Schreier, A. Wallraff, J. M. Gambetta, A. Blais, L. Frunzio, J. Majer, B. Johnson, M. H. Devoret, et al., Nature **445**, 515 (2007).
[16] D. I. Schuster, A. Wallraff, A. Blais, L. Frunzio, R. S. Huang, J. Majer, S. M. Girvin, and R. J. Schoelkopf, Phys. Rev. Lett. **98**, 049902 (2007).
[17] J. Majer, J. M. Chow, J. M. Gambetta, J. Koch, B. R. Johnson, J. A. Schreier, L. Frunzio, D. I. Schuster, A. A. Houck, A. Wallraff, et al., Nature **449**, 443 (2007).
[18] A. A. Houck, D. I. Schuster, J. M. Gambetta, J. A. Schreier, B. R. Johnson, J. M. Chow, L. Frunzio, J. Majer, M. H. Devoret, S. M. Girvin, et al., Nature **449**, 328 (2007).
[19] O. Astafiev, K. Inomata, A. O. Niskanen, T. Yamamoto, Y. A. Pashkin, Y. Nakamura, and J. S. Tsai, Nature **449**, 588 (2007).
[20] M. A. Sillanpää, J. I. Park, and R. W. Simmonds, Nature **449**, 438 (2007).
[21] M. Hofheinz, E. M. Weig, M. Ansmann, R. C. Bialczak, E. Lucero, M. Neeley, A. D. O'Connell, H. Wang, J. M. Martinis, and A. N. Cleland, Nature p. 310 (454).
[22] J. M. Fink, M. Göppl, M. Baur, R. Bianchetti, P. J. Leek, A. Blais, and A. Wallraff, Nature **454**, 315 (2008).
[23] A. Blais, R.-S. Huang, A. Wallraff, S. M. Girvin, and R. J. Schoelkopf, Phys. Rev. A **69**, 062320 (2004).
[24] R. Schoelkopf and S. Girvin, Nature **451**, 664 (2008).
[25] L. Frunzio, A. Wallraff, D. Schuster, J. Majer, and R. Schoelkopf, IEEE Trans. Appl. Supercond. **15**, 860 (2005).
[26] J. Baselmans, R. Barends, J. Hovenier, J. Gao, H. Hoevers, P. de Korte, and T. Klapwijk, Bull. Soc. Roy. Sci. Liège **74**, 5 (2005).
[27] R. Barends, J. Baselmans, J. Hovenier, J. Gao, S. Yates, T. Klapwijk, and H. Hoevers, IEEE Trans. Appl. Supercond. **17(2)**, 263 (2007).
[28] A. D. O'Connell, M. Ansmann, R. C. Bialczak, M. Hofheinz, N. Katz, E. Lucero, C. McKenney, M. Neeley, H. Wang, E. M. Weig, et al., arXiv.org:0802.2404 (2008).
[29] J. A. Schreier, A. A. Houck, J. Koch, D. I. Schuster, B. R. Johnson, J. M. Chow, J. M. Gambetta, J. Majer, L. Frunzio, M. H. Devoret, et al., Phys. Rev. B 77 **77**, 180502 (2008).
[30] P. Rabl, D. DeMille, J. M. Doyle, M. D. Lukin, R. J. Schoelkopf, and P. Zoller, Phys. Rev. Lett. **97**, 033003 (2006).
[31] *VeriCold Technologies*, URL `http://www.vericold.com`.
[32] B. Abdo, E. Segev, O. Shtempluck, and E. Buks, Phys. Rev. B **73**, 11 (2006).
[33] J. M. Martinis, K. B. Cooper, R. McDermott, M. Steffen, M. Ansmann, K. D. Osborn, K. Cicak, S. Oh, D. P. Pappas, R. W. Simmonds, et al., Phys. Rev. Lett. **95**, 210503 (2005).
[34] S. Gevorgian, L. J. P. Linnér, and E. L. Kollberg, IEEE Trans. Microwave Theory Techn. **43(2)**, 772 (1995).
[35] K. Watanabe, K. Yoshida, T. Aoki, and S. Kohjiro, Jap. J. Appl. Phys. **33**, 5708 (1994).
[36] E. Chen and S. Chou, IEEE Trans. Microwave Theory Techn. **45(6)**, 939 (1997).
[37] J. Musil, *Microwave Measurements of Complex Permittivity by Free Space Methods and Their Applications* (Elsevier, 1986).
[38] M. Tinkham, *Introduction to Superconductivity* (McGraw-Hill International Editions, 1996).
[39] R. Parks, *Superconductivity Vol.2* (Marcel Dekker, Inc., New York, 1969).
[40] C. P. Poole, *Superconductivity* (Academic Press Inc.,U.S, 1995).
[41] D. M. Pozar, *Microwave Engineering* (Addison-Wesley Publishing Company, 1993).
[42] J. Browne, Microw. RF **26(2)**, 131 (1987).